

From liquid to solid bonding in cohesive granular media

Jean-Yves Delenne*, Fabien Soulié, Moulay Saïd El Youssofi and Farhang Radjai

April 26, 2022

Abstract

We study the transition of a granular packing from liquid to solid bonding in the course of drying. The particles are initially wetted by a liquid brine and the cohesion of the packing is ensured by capillary forces, but the crystallization of the solute transforms the liquid bonds into partially cemented bonds. This transition is evidenced experimentally by measuring the compressive strength of the samples at regular intervals of times. Our experimental data reveal three regimes: 1) Up to a critical degree of saturation, no solid bonds are formed and the cohesion remains practically constant; 2) The onset of cementation occurs at the surface and a front spreads towards the center of the sample with a nonlinear increase of the cohesion; 3) All bonds are partially cemented when the cementation front reaches the center of the sample, but the cohesion increases rapidly due to the consolidation of cemented bonds. We introduce a model based on a parametric cohesion law at the bonds and a bond crystallization parameter. This model predicts correctly the phase transition and the relation between microscopic and macroscopic cohesion.

keywords: Unsaturated granular media, capillarity, cementation, DEM, compressive strength

PACS: 45.40.-f; 45.70.Mg; 81.05.Rm

1 Introduction

Granular materials occur very often in nature and industrial applications with liquid or solid bonds between the particles. The effect of capillary bonding on the mechanical behavior of granular materials is of primary importance in powder technology [1, 2, 3] and transformations of geomaterials [4, 5, 6]. Capillary bonding has been extensively studied in the past, and several models of capillary cohesion have been proposed [7, 12, 8]. The scale-up of capillary forces to the macroscopic cohesion of granular media has been investigated by means of both experiments and discrete element numerical simulations [13, 14, 15].

*Corresponding author: delenne@lmgc.univ-montp2.fr; Laboratoire de Mécanique et Génie Civil, CNRS - Université Montpellier 2, Place Eugène Bataillon, 34095 Montpellier cedex 05

In the same way, solid bonding is found in various materials such as sedimentary rocks (sandstones, conglomerates and breccia)[24], biomaterials such as wheat endosperm (starch granules forming a compact structure bound together by a protein matrix) [26, 28], and geomaterials like mortars, concrete and asphalt (aggregates of various sizes glued to each other by a cement paste) [27]. The cohesive behavior due to solid bonds between the particles and the rupture of cemented granular materials have been recently investigated by several authors [9, 10, 25].

There is a broad class of processes where the nature of cohesive bonds evolves from solid to liquid and vice versa. The liquid is generally water with various types of impurities and/or dissolved minerals. As a result of reactive transfers or phase transitions, the liquid may influence the mechanical properties by dissolution of cemented joints or crystallization of solutes. The mechanical properties can thus evolve in response to external hygrothermic conditions [8]. In pharmaceutical industry, for example, the process of wet granulation is widely used to manufacture tablets. A liquid composed of solvent(s) and solute(s) is mixed with dry powder in order to obtain a homogeneous mixture that would segregate in the absence of the liquid. The formation of aggregates in the process of mixing has been a subject of extensive investigation [1, 2, 3]. The solid tablets are obtained by drying: the solvent evaporates and solid bridges are formed between grains by crystallization, thus ensuring the macroscopic cohesion of the tablets.

In this paper, we are interested in the evolution of the macroscopic cohesion of a wet granular material during the evaporation of a solvent (water) and thus crystallization of the solute (sodium chloride). At low liquid contents, the water is in the form of capillary bridges between particles. The hydrous field corresponding to this range of liquid contents is often described as “pendular”. The attractive capillary forces in the presence of liquid bridges between particles endows the material with macroscopic cohesion [8, 29]. Under the action of the surrounding hygrothermic conditions, the water evaporates and the solutes crystallize to form solid bonds between grains. The cohesion is initially of capillary origin but begins to increase as soon as the first solid bonds are formed at the free boundary of the sample and a solidification front propagates from the boundary to the center of the sample.

We measure the compressive strength of several samples of glass beads and sand, prepared in the pendular state by mixing with a saturated brine, in the course of drying. Technically, it is not trivial to follow simultaneously the evolution of the internal state due to the evaporation of the brine and the evolution of its mechanical behavior. Moreover, the two limits of purely liquid bonding and purely solid bonding have different behaviors and require specific experimental tools and precautions. For these reasons, the experimental campaign involves the preparation of many reproducible samples subjected to identical drying conditions, each sample being destroyed when subjected to simple compression test.

We show that the evolution of the cohesion is governed by three time scales corresponding to the evaporation of a single capillary bridge, the propagation of the cementation front from the surface to the center and the aging of cemented

bonds. These time scales are identified from the experimental campaign together with a theoretical model based on a simple representation of the evolution of the debonding force between the particles. This model fits well the compressive strength as a function of an order parameter representing the state of crystallization.

In the following, we first describe in section 2 the experimental setup, the procedures of sample preparation and the main results regarding the evolution of the samples and mechanical strength in the course of drying. In section 3, we present our model and compare its predictions with the experimental data. We conclude with a summary and scopes of this work.

2 Experiments

2.1 Experimental setup

The experimental tests were designed to measure the compressive strength of granular samples during the process of the drying and deposition of a solute at the liquid bridges between the grains. Two types of materials were used in these tests: (1) a model material composed of glass beads and (2) a natural material: Ventoux sand. In both cases, the grains were first washed and dried. Then, they were sieved to keep only the grains with diameters in the range from 0.4 mm to 0.8 mm. The dry grains were homogeneously mixed with a small amount of saturated brine containing 35.6 g of NaCl for 100 g of water in controlled environment (temperature, humidity). This maximum concentration varies with temperature [17, 18].

The samples (diameter 25 mm and height 17 mm) were prepared inside a cylindrical mould. At this stage, the samples are particularly delicate to handle since their mechanical strength is solely ensured by weak capillary forces acting between the grains. Because of this brittleness, particular experimental precautions were necessary in order to avoid damage to the samples upon un moulding.

Each sample is initially a three-phase material including

- a solid phase (denoted by S) composed of grains (glass beads or sand) with a total mass m_{grains}^S ,
- a liquid phase (denoted by L) composed of water of mass $m_{H_2O}^L$ and dissolved NaCl of mass m_{NaCl}^L .
- a gaseous phase composed of air and water vapor with negligible mass compared to the two other phases but which carries the kinetics of drying.

Thus, the total mass of the sample at this initial state is $m_i = m_{H_2O}^L + m_{NaCl}^L + m_{grains}^S$.

The water evaporates at the surface and causes thermodynamic disequilibrium of the solution. The equilibrium is recovered through the crystallization of NaCl and thus the formation of solid NaCl deposits of a total mass m_{NaCl}^S . A

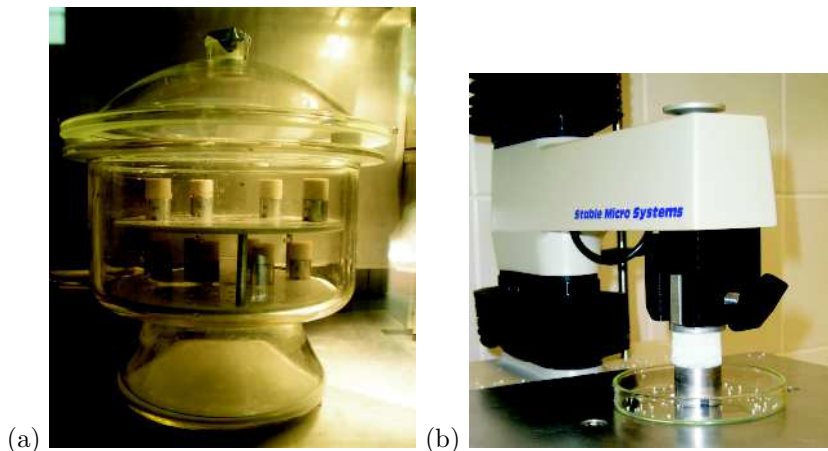


Figure 1: (a) Photograph of the sample in the process of drying; (b) The press used for the unconfined compression tests.

crystallization front propagates thus from the boundary towards the center of the sample. The evolution of a sample is expected to be governed by the ratio

$$I_c = \frac{m_{NaCl}^S}{m_{NaCl}^S + m_{NaCl}^L} \quad (1)$$

to which we refer as the global crystallization index of the sample.

Three series of samples were prepared with three different values of the initial liquid content $w_{Li} \equiv (m_{H_2O}^L + m_{NaCl}^L)/m_{grains}^S$: 3 %, 5 % and 7 %. These values were selected in the hydrous field corresponding to the “pendular state” where liquid bridges between grains ensure the mechanical integrity of the sample. The samples were weighed just after preparation, and left to dry at constant temperature $T = 20^\circ \text{C}$ and relative humidity $RH = 43 \%$ for drying times varying from 15 minutes to 18 hours; see Fig. 1(a).

At regular intervals of time, the samples were weighed (mass m_f), and then subjected to unconfined vertical compression up to failure. The tests were carried out by means of a “low capacity” press, which allows us to test samples with low dimensions and forces up to 50 N with an accuracy of 0.01 N; see Fig. 1(b). The difference $m_f - m_i$ yields the mass of the evaporated water and thus that of the crystallized mass fraction of NaCl. Since all samples are prepared under similar conditions, they are assumed to follow the same evolution in time. This allows us to reconstruct the kinetics of crystallization.

2.2 Experimental results

The evolution of the compressive stress σ^Y at yield is shown in Fig. 2 as a function of the global crystallization index I_c for glass beads and sand, as well as from a theoretical model described in section 3. All the experimental data

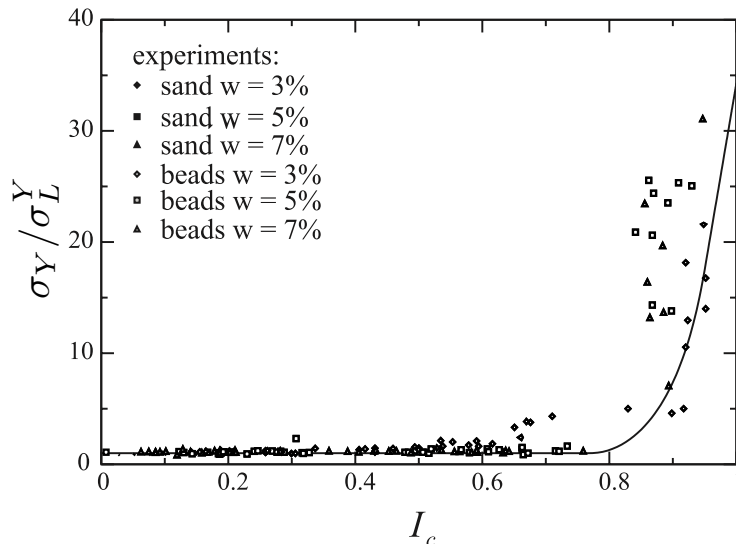


Figure 2: Compressive yield stress σ^Y , normalized by the yield stress σ_L^Y due only to capillary forces (yield stress in the first regime) as a function of the global crystallization index I_c in experiments. The solid line corresponding to theoretical model (see section 3) is plotted as a guide to eyes.

collapse nearly on the same curve for glass beads and sand. We distinguish three regimes in the evolution of the cohesion. As long as I_c is below a threshold I_T , the yield stress is independent of I_c . In this regime, the amount of the crystallized salt at the boundary layer of the sample, where the whole process is initiated due to exchange with the atmosphere, is insufficient to allow for the formation of solid bonds between the particles. Therefore, the yield stress σ^Y in this regime is only due to the capillary bonds between the particles. In Fig. 2, we see that σ^Y is independent both of the initial liquid content w_{Li} and of the type of grains. In fact, both experiments and theoretical analysis suggest that in a homogeneously wetted granular material in the pendular state, the capillary cohesion is practically independent of the liquid content but crucially depends on the number density of the capillary bonds [29].

The yield stress increases from $I_c \simeq 0.9$ due to the partial cementation of the first bonds at the boundary of the sample and the propagation of a solidification front towards the center of the sample. The yield stress increases rapidly in this regime. A photograph of the cementation front in a partially dried sample is displayed in Fig. 3. The bonds in the central part of the sample were of capillary type and thus the grains were easily removed. The remaining grains form a solid crown due to cemented bridges between the particles. Hence, the thickness of this crown represents the distance run by the solidification front. It should be noted that the solid bonds behind this front are only partially cemented. At this stage, each solid bond is composed of a crystallized superficial layer with



Figure 3: Photograph of a partially dried sample in the second regime.

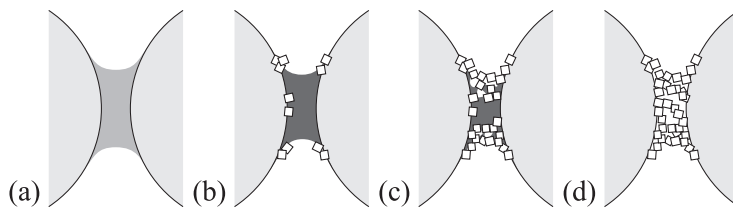


Figure 4: Schematic representation of the evolution of bridge: from a liquid to a solid bridge.

liquid brine inside. As drying continues, the cemented bond gets thicker and stronger until the whole bond solidifies. This process is illustrated in Fig. 4.

All bonds are cemented when the center of the sample is reached by the cementation front. In this third regime, σ^Y rises linearly to a level as high as 35 times the capillary yield stress due to the consolidation of the cemented bonds throughout the system as a result of continued crystallization of the brine at each bond. These high values of compressive strength as $I_c \rightarrow 1$ has two different origins. On one hand, the debonding force of a solid NaCl bond is nearly 7 times that of a capillary bond. On the other hand, unlike a liquid bond which involves only a tensile strength in addition to sliding friction, a solid bond has a rolling (or bending) strength as well as a tensile strength. This rolling strength is crucial for the compressive strength of cohesive granular materials [21, 23].

Figure 5 shows the evolution of I_c with time t . This evolution reflects the kinetics of drying with the transport of water in the gas phase. I_c begins to increase as soon as the sample is exposed, but the first partially cemented bonds

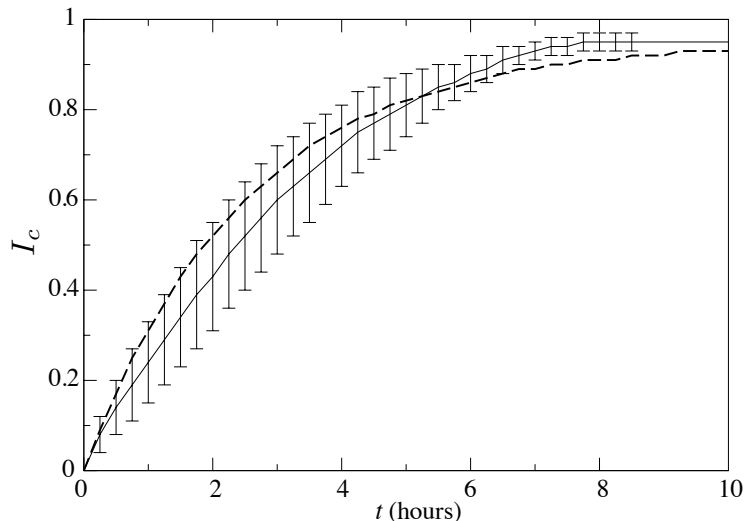


Figure 5: Evolution of the global crystallization index with time; solid line: experimental results, dotted line: model equation (2). The error bars represent the standard deviation for five independent experiments.

are completely formed only at $I_c = I_T \simeq 0.9$. Then, I_c increases mainly due to the formation of the first (partially) cemented bonds followed by the propagation of the cementation front into the sample. When this front reaches the center of the sample, I_c increases only due to the aging and consolidation of the cemented bonds. Although the kinetics of drying is not exactly the same in each regime, the time evolution of I_c is quite well fit by an exponentially increasing function:

$$I_c(t) = 1 - e^{-\frac{t}{t_d}} \quad (2)$$

where t_d is a characteristic drying time. This form suggests that the drying rate is proportional to the residual liquid.

3 Model

The evolution of the compressive strength may be understood on quantitative grounds by considering 1) a local cohesion law involving the phase change from liquid to solid at the level of a single bond, 2) the relation between the bond strength and the macroscopic strength, and 3) the kinetics of drying both at the surface and in the bulk. In the following, we present a model that is based on these ingredients and correctly captures the macroscopic evolution as shown by the fitting form in Fig. 2.

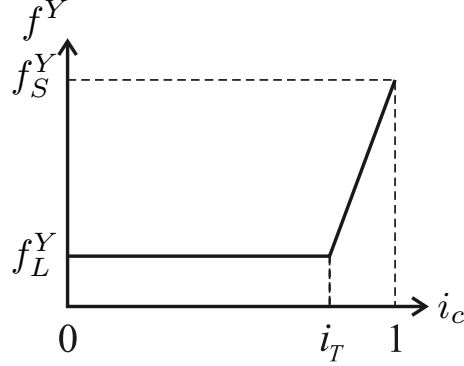


Figure 6: The parametric adhesion law.

3.1 Single-bond behavior

The phase change of a bond from liquid to solid is controlled by the amount of the deposited solute. Hence, the natural control parameter for phase transition at this scale is the bond crystallization index i_c defined by

$$i_c = \frac{m_{NaCl}^S(\text{bond})}{m_{NaCl}^S(\text{bond}) + m_{NaCl}^L(\text{bond})} \quad (3)$$

This index depends on the history of the bond and is thus a function $i_c(r, t)$ of the radial position r of the bond and the time t elapsed since the beginning of drying. We assume translational invariance along the axis of the sample. The index i_c varies between 0 for a liquid bond and 1 for a fully cemented bond. The transition from liquid to solid takes place at a particular value $i_c = i_T$ which corresponds to the deposition of the first percolating shell of crystallized solute across the gap or at contact between two particles. In this transition, the tensile force threshold f^Y (the debonding force) increases from that of a liquid bond f_L^Y to that of a fully cemented bond f_S^Y . We have $f^Y = f_L^Y$ for $0 \leq i_c \leq i_T$ and $f^Y = f_S^Y$ for $i_c = 1$. Assuming a linear evolution between these two limits, we get the following *parametric* adhesion law:

$$f^Y = f_L^Y + H(i_c - i_T) \frac{i_c - i_T}{1 - i_T} (f_S^Y - f_L^Y) \quad (4)$$

where H is the Heaviside step function. A plot of this relation is shown in Fig. 6.

Remark that f^Y in equation 4 is the force threshold and the actual value of the normal force f_n depends on the force law expressing a force-displacement relation. This relation is different for a liquid bond and a partially or fully cemented bond. Several expressions have been proposed for the capillary force f_L as a function of the gap δ , bond liquid volume V_b and surface tension γ [8, 29]. The capillary force has its largest value at the contact between two

particles and declines exponentially with the gap:

$$f_L = 2\pi\gamma \cos\theta \rho e^{-\delta/\lambda}, \quad (5)$$

where λ is a characteristic length depending on V_b and the particle radii, ρ is a reduced length depending on the particle radii and θ is the contact angle [12, 31, 32]. A capillary bridge is stable as long as $\delta < \delta^{max}$ given by [33]

$$\delta^{max} = \left(1 + \frac{\theta}{2}\right) V_b^{1/3}. \quad (6)$$

This distance is small (compared to λ) in the pendular state and in practice the debonding force can be approximated by

$$f_L^Y = 2\pi\gamma \cos\theta \rho \quad (7)$$

This force is independent of the bond liquid volume V_b .

The fully cemented bonds have a brittle behavior with a debonding threshold $f_S^Y \simeq 7f_L^Y$ for the three values of w_{Li} used in our experiments. The behavior is also brittle for the partially cemented bonds with a threshold which is assumed here to vary linearly with the bond crystallization index according to equation 4. Obviously, the cemented bonds exhibit also a shear strength and a rolling strength in addition to the tensile strength considered above. This feature, which differentiates cemented bonds from liquid bonds, is not considered explicitly in the single-bond behavior but will be taken into account through a Coulomb cohesion parameter c at the macroscopic scale.

3.2 From single bond to RVE

A schematic representation of our model is shown in Fig. 7. It consists of two scales: 1) The microscopic or local scale is defined by the parametric adhesion law $f^Y\{i_c(r, t)\}$; 2) The macroscopic or global scale is characterized by the relation $\sigma^Y\{I_c(t)\}$. Given the local adhesion law, the macroscopic behavior can be determined from the relationships between i_c and I_c , on one hand, and between f^Y and σ^Y , on the other hand. We first consider a Representative Volume Element (RVE). Then, solve the problem in the presence of hydric gradients in the drying process by introducing a simple propagation equation for the local crystallization index.

We assume a homogeneous distribution of the liquid bonds in the initial preparation of the sample. We also assume that the total mass of NaCl is the same for all bonds. Then, the macroscopic crystallization index is simply the volume average of the bond crystallization index:

$$I_c(t) = \langle i_c(r, t) \rangle_V = \frac{h}{V} \int_0^R 2\pi r i_c(r, t) dr \quad (8)$$

where h and R are the height and radius of the sample, respectively, and $V = \pi R^2 h$ is its volume. According to equation 8, for a RVE and in the absence

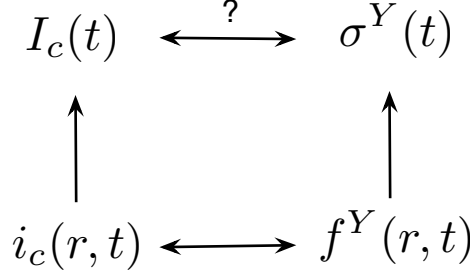


Figure 7: Diagram of microscopic model and upscaling method.

of hydric gradients, we have $I_T = i_T$ since all bonds reach simultaneously this point. During drying, the cementation is initiated at the surface of the sample for $i_c = i_T$ and we have $i_c < i_T$ everywhere in the bulk.

In order to propose a relation between f^Y and σ^Y , we need to postulate the deformation mechanism, the macroscopic failure mode and the general expression of the stress tensor in a granular material as a function of the bond forces. The stress tensor σ_{ij} is the first moment of the bond forces f_i averaged over the control volume V [23, 30]:

$$\sigma_{ij} = n_b \langle f_i \ell_j \rangle_V \quad (9)$$

where n_b is the number density of the bonds and ℓ_j is the j -component of the branch vector joining the centers of the two particles at contact. The averaging runs over all contacts belonging to the control volume. Assuming that the branch vector lengths and forces are not correlated and for a medium with uniformly distributed branch vectors in all directions, the normal stress σ_n is given by

$$\sigma_n = \frac{1}{3} n_b \langle \ell \rangle \langle f_n \rangle \quad (10)$$

where f_n is the normal bond force. We have $\langle f_t \rangle \simeq 0$ as a result of the balance of force moments on each particle.

According to equation 10, the maximum tensile force σ_n^{max} in a RVE is obtained by replacing f_n by f^Y :

$$\sigma_n^{max} = \frac{1}{3} n_b \langle \ell \rangle \langle f^Y \rangle \quad (11)$$

Assuming that the Mohr-Coulomb failure criterion holds in the tensile regime, the Coulomb cohesion c is thus simply given by

$$c = \mu \sigma_n^{max} = \frac{1}{3} n_b \tan \varphi \langle \ell \rangle \langle f^Y \rangle \quad (12)$$

where μ is the friction coefficient and φ is the friction angle.

Finally, we need the relation between the axial stress σ_1 and the cohesion c in order to evaluate the compressive strength. Under the conditions of axial

symmetry, we have $\sigma_2 = \sigma_3$. Let $p = (\sigma_1 + 2\sigma_3)/3$ and $q = (\sigma_1 - \sigma_3)/3$ be the mean stress and stress deviator, respectively. At failure, we have

$$\frac{q}{p} = \frac{2}{3 - \sin \varphi} \left(\sin \varphi + \frac{c}{p} \cos \varphi \right) \quad (13)$$

In our experiments the confining stress is zero: $\sigma_2 = \sigma_3 = 0$. Hence, from equation (13), at failure we have

$$\sigma_1 = \sigma^Y = 2c \frac{\cos \varphi}{1 - \sin \varphi} \quad (14)$$

Finally, the substitution of c from equation 12 yields

$$\sigma^Y = \frac{2}{3} n_b \langle \ell \rangle \frac{\sin \varphi}{1 - \sin \varphi} \langle f^Y \rangle \quad (15)$$

Equation (15) shows that the compressive strength is proportional to the microscopic force threshold and to the number density of the bonds. Notice that n_b is simply half the average number of bonds per particle divided by the free volume, i.e. the mean volume V_p of a Voronoi cell surrounding the particle:

$$n_b = \frac{z}{2V_p} \quad (16)$$

By definition, given the solid fraction ϕ of the sample, $V_p \phi$ is the mean volume of a particle. Thus,

$$V_p = \frac{\pi \langle d^3 \rangle}{6\phi} \quad (17)$$

where d is the particle diameter. For nearly spherical particles, we may set $\langle \ell \rangle \simeq \langle d \rangle$. From equations (15), (16) and (17), we get the following equation in which the prefactor to f^Y is expressed in terms of the familiar parameters:

$$\sigma^Y = \frac{2}{\pi} z \phi \frac{\sin \varphi}{1 - \sin \varphi} \frac{\langle d \rangle}{\langle d^3 \rangle} \langle f^Y \rangle \quad (18)$$

For the typical values $z = 6$, $\varphi = \pi/6$ and $\phi = 0.6$ and assuming monodisperse particles, we get $\sigma^Y \simeq 2f^Y/d^2$, which is a simple relation.

3.3 Compressive strength

From the relations (8) and (18) together with the parametric adhesion law (4), it is straightforward to predict the macroscopic behavior. We first take the average of both sides of equation (4):

$$\langle f^Y \rangle = f_L^Y + \frac{f_S^Y - f_L^Y}{1 - i_T} \langle (i_c - i_T) H(i_c - i_T) \rangle \quad (19)$$

where the averaging runs over the whole sample. Inserting this expression of the mean force threshold in equation (18), we get

$$\sigma^Y = \frac{2}{\pi} z \phi \frac{\sin \varphi}{1 - \sin \varphi} \frac{\langle d \rangle}{\langle d^3 \rangle} \left\{ f_L^Y + \frac{f_S^Y - f_L^Y}{1 - i_T} \langle (i_c - i_T) H(i_c - i_T) \rangle \right\} \quad (20)$$

The average $\langle (i_c - i_T) H(i_c - i_T) \rangle_V$ in the right hand side of equation (20) depends on the function $i_c(r, t)$ and will be evaluated below in the presence of a hydric gradient. Here, we consider the first and third regimes identified in the experiments (see section 2.2). The first regime corresponds to the initial stage of drying where $i_c(r, t) < i_T$ for all bonds and no cemented bond is formed. Hence, according to (20), the compressive strength in this regime is given by

$$\sigma^Y = \sigma_L^Y = \frac{2}{\pi} z \phi \frac{\sin \varphi}{1 - \sin \varphi} \frac{\langle d \rangle}{\langle d^3 \rangle} f_L^Y \quad (21)$$

We see that σ^Y in this regime is constant and independent of I_c . The purely liquid-bond strength σ_L^Y can be used to scale σ^Y in equation (20):

$$\frac{\sigma^Y}{\sigma_L^Y} = 1 + \frac{f_S^Y / f_L^Y - 1}{1 - i_T} \langle (i_c - i_T) H(i_c - i_T) \rangle \quad (22)$$

In the third regime, the cementation front has reached the center of the sample and we have $i_T \leq i_c(r, t)$, and thus $H(i_c - i_T) = 1$ everywhere. As a result, from equations (8) and (22) we get

$$\frac{\sigma^Y}{\sigma_L^Y} = 1 + \frac{f_S^Y / f_L^Y - 1}{1 - i_T} (I_c - i_T) \quad (23)$$

This equation shows that in the last stage of drying, corresponding to the consolidation of all bonds, the compressive strength increases linearly with I_c . This linear behavior and the predicted value of the coefficient $\frac{f_S^Y / f_L^Y - 1}{1 - i_T} \simeq 30$ for $f_S^Y / f_L^Y \simeq 7$ and $i_T \simeq 0.9$ are consistent with the data shown in Fig. 2 within our experimental precision.

3.4 Cementation front

The second regime is a transient beginning with the cementation of the bonds located at the surface and ending when all bonds are partially cemented. In this regime, the bonds at a radial position $r < r_T(t)$ are liquid whereas the bonds with $r_T(t) \leq r$ are partially cemented. The cementation front $r_T(t)$ decreases from R at the end of the first regime to 0 at the beginning of the third regime. By definition, we have $i_c(r = r_T, t = t_T) = i_T$.

For the evaluation of the compressive strength in the second regime, we need the function $i_c(r, t)$. By definition, $1 - i_c(r, t)$ is the proportion of the liquid brine in the bond, which is conserved in the bulk: The time variation $\partial_t \{1 - i_c(r, t)\}$ of the liquid in the bonds located at r is compensated by a flux J in the vapor

phase. Assuming that J is proportional to the gradient $\partial_r\{1-i_c(r,t)\}$, we arrive at a diffusion equation for i_c :

$$\frac{\partial i_c}{\partial t} = D \left\{ \frac{\partial^2 i_c}{\partial r^2} + \frac{1}{r} \frac{\partial i_c}{\partial r} \right\} \quad (24)$$

where invariance by rotation around the axis and by translation along the axis are assumed, and D is a diffusion coefficient.

Evaporation takes place only radially and at the free surface $r = R$. The exponential increase of I_c observed in the experiments (see Fig. 5) suggests a simple exponential time evolution of $i_c(r = R, t)$:

$$i_c(R, t) = 1 - e^{-\beta t/t_T} \quad (25)$$

The characteristic time t_T represents the time necessary for the onset of cementation in a bond when $i_c = i_T$. We have $i_T = 1 - e^{-\beta}$. Hence, equation (25) can be rewritten in the following form

$$i_c(R, t) = 1 - (1 - i_T)^{t/t_T} \quad (26)$$

Equation (24) can be solved with (26) as its boundary value for an initially homogeneous system in which $i_c(r, t = 0) = 0$ for all $r \neq R$. The solution is [22]

$$i_c(r, t) = \{1 - (1 - i_T)^{t/t_T}\} \left\{ 1 - \frac{2}{R} \sum_{n=1}^{\infty} \frac{e^{-D\alpha_n^2 t} J_0(\alpha_n r)}{\alpha_n J_1(\alpha_n R)} \right\} \quad (27)$$

where J_0 and J_1 are Bessel functions of the first kind of order zero and one, respectively, and α_n is the n^{th} root of the equation $\alpha J_1(\alpha R) = J_0(\alpha R)$. The solution (eq. 27) is displayed on Fig. 8.

From equation (27) we can calculate the global crystallization index defined by (8):

$$I_c(t) = \frac{2}{R^2} \int_0^R r i_c(r, t) dr = \{1 - (1 - i_T)^{t/t_T}\} \left\{ 1 - \frac{4}{R^2} \sum_{n=1}^{\infty} \frac{e^{-D\alpha_n^2 t}}{\alpha_n^2} \right\} \quad (28)$$

The macroscopic transition index I_T is the value of I_c at $t = t_T$. Hence

$$I_T = i_T \left\{ 1 - \frac{4}{R^2} \sum_{n=1}^{\infty} \frac{e^{-D\alpha_n^2 t_T}}{\alpha_n^2} \right\} \quad (29)$$

This relation implies that $I_T < i_T$. Given the high value of t_T , in practice we have $I_T \simeq i_T$.

Equation (27) is an implicit equation for the cementation front $r_T(t)$ defined by the condition $i_c(r_T, t) = i_T$. The knowledge of $r_T(t)$ allows us to determine the total compressive strength σ^Y as the weighted mean of σ_L^Y in the region $r < r_T$ and σ_S^Y in the region $r_T < r$:

$$\sigma^Y(t) = \frac{r_T^2(t)}{R^2} \sigma_L^Y + \left\{ 1 - \frac{r_T^2(t)}{R^2} \right\} \sigma_S^Y \quad (30)$$

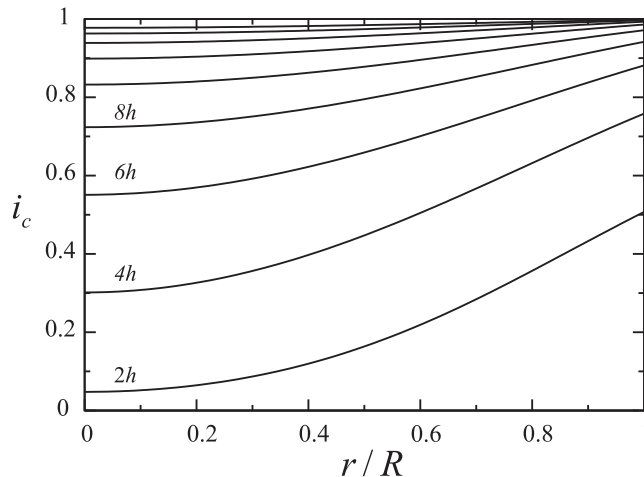


Figure 8: Evolution of the local crystallisation index i_c in the bulk with time.

Plugging the expressions (21) and (22) into equation (30) yields

$$\frac{\sigma^Y}{\sigma_L^Y} = 1 + \left\{ 1 - \frac{r_T^2(t)}{R^2} \right\} \frac{f_S^Y/f_L^Y - 1}{1 - i_T} (I_c - i_T) \quad (31)$$

where i_T may be replaced by I_T from equation 29.

Equation (31) holds only in the second regime, but we retrieve the expression of σ_S^Y in equation (22) for the third regime by setting $r_T = 0$ as well as the first regime by setting $r_T = R$ (equation (22)). The nonlinear increase of σ^Y in the second regime with I_c is given by the factor $1 - r_T^2/R^2$. This corresponds to a first-order phase transition at the macroscopic scale for I_c as control parameter and σ^Y as state parameter.

The model described in this section is able to predict the global crystallization index $I_c(t)$ as a function of time (equation (1)) and the compressive strength $\sigma^Y(I_c)$ as a function of I_c (equations (31), (22) and (22)). The plots of these functions for the experimental parameters are displayed in figures 5 and 2. The predicted behavior is thus fairly good within the available experimental precision. Apart from the radius R of the sample, for these fits three parameters were used from experimental measurements, namely i_T , D and t_T . The good estimation of σ_L^Y provides a strong support for our model.

4 Conclusion

In this paper, we introduced a simple experimental setup allowing us to analyze the transition from capillary cohesion to solid cohesion induced by surface drying and the progressive crystallization of a liquid brine wetting initially the particles. This transition was evidenced experimentally by measuring the com-

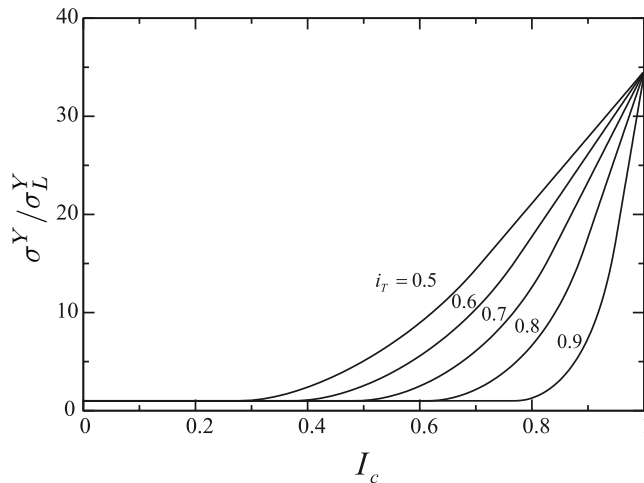


Figure 9: Influence of the local transition index on the compression strength as a function of the macroscopic crystallisation index I_c .

pressive strength of the samples in the course of time, and modeled by introducing the relevant variables both at the scale of a bond and at the macroscopic scale. Three regimes were evidenced: 1) the capillary regime as long as the degree of saturation remains below a critical value; 2) the transition regime, corresponding to the initiation and propagation of a cementation front spreading towards the center of the sample, and 3) the cemented regime, where all bonds are partially solidified but continue to strengthen due to further crystallization. The predicted behavior by our theoretical model is in good agreement with the experimental data. This model, based on an evolutive cohesion law at the bonds, takes into account the kinetics of crystallization and the granular texture. It correctly predicts the compressive strength in the capillary and cemented regimes.

The framework of the model presented in this work is quite general. It can be applied to granular materials subjected to evolutive force laws or phase compositions. For example, the degradation of a geomaterial under the action of progressive dissolution of solid bonds in a humid environment bears strong similarity with the problem treated in this paper.

References

- [1] S. Iveson, J. Litster, B. Ennis, Fundamental studies of granule consolidation. part 1: Effects of binder content and binder viscosity, *Powder Technology* 88 (1996) 15–20.
- [2] S. Iveson, J. Litster, K. Hapgood, B. Ennis, Nucleation, growth and breakage phenomena in agitated wet granulation processes: A review, *Powder Technology* 117 (2001) 3–39.
- [3] A. Nokhodchi, An overview of the effect of moisture on compaction and compression, *Pharmaceutical Technology* 29 (1) (2005) 46–66.
- [4] C. Cardell, F. Delalieux, K. Roumpopoulos, A. Moropoulou, F. Auger, R. V. Grieken, Salt-induced decay in calcareous stone monuments and buildings in a marine environment in SW france, *Construction and Building Materials* 17 (2003) 165–179.
- [5] B. Lubelli, R. V. Hees, C. Groot, The role of sea salts in the occurrence of different damage mechanisms and decay patterns on brick masonry, *Construction and Building Materials* 18 (2004) 119–124.
- [6] L. Rijniens, L. Pel, H. Huinink, K. Kopinga, Salt crystallization as damage mechanism in porous building materials—a nuclear magnetic resonance study, *Magnetic Resonance Imaging* 23 (2005) 273–276.
- [7] T. Mikami, H. Kamiya, M. Horio, Numerical simulation of cohesive powder behavior in a fluidized bed, *Chemical Engineering Science* 53 (10) (1998) 1927–1940.
- [8] F. Soulié, F. Cherblanc, M. S. El Youssoufi, C. Saix, Influence of liquid bridges on the mechanical behaviour of polydisperse granular materials, *International Journal for Numerical and Analytical Methods in Geomechanics* 30 (2006) 213–228.
- [9] J.-Y. Delenne, M. S. El Youssoufi, F. Cherblanc, J.-C. Béné, Mechanical behaviour and failure of cohesive granular materials, *International Journal for Numerical and Analytical Methods in Geomechanics* 28 (2004) 1577–1594.
- [10] J.-Y. Delenne, Y. Haddad, J.-C. Benet, J. Abecassis. Use of mechanics of cohesive granular media for analysis of hardness and vitreousness of wheat endosperm, *Journal of Cereal Science*, 47 (2008) 438–444.
- [11] F. Soulié, M. S. El Youssoufi, J.-Y. Delenne, C. Voivret, C. Saix, Effect of the crystallization of a solute on the cohesion in granular materials, *Powder Technology* 175 (2007) 43–47.
- [12] C. Willett, M. Adams, S. Johnson, J. Seville, Capillary bridges between two spherical bodies, *Langmuir* 16 (2000) 9396–9405.

- [13] X. Pepin, S. Simons, S. Blanchon, D. Rossetti, G. Couarraze, Hardness of moist agglomerates in relation to interparticle friction, granule liquid content and nature, *Powder Technology* 117 (1-2) (2001) 123–138.
- [14] T. Kim, C. Hwang, Modeling of tensile strength on moist granular earth material at low water content, *Engineering Geology* 69 (2150) (2003) 233–244.
- [15] V. Richefeu, M. S. E. Youssoufi, F. Radjai, Shear strength properties of wet granular materials, *Physical Review E* 73 (051304) (2006) 1–11.
- [16] L. Farber, G. Tardos, J. Michaels, Evolution and structure of drying material bridges of pharmaceutical excipients: Studies on a microscope slide, *Chemical Engineering Science* 58 (2003) 4515–4525.
- [17] D. Kaufmann (Ed.), *Sodium chloride, the production and properties of salt and brine*, Reinhold Publishing Corporation, New York, 1960.
- [18] H. Langer, H. Offermann, On the solubility of sodium chloride in water, *Crystal Growth* 60 (1982) 389–392.
- [19] C. Rodriguez-Navarro, E. Doehne, Salt weathering : Influence of evaporation rate, supersaturation and cristallization pattern, *Irrigation and drainage* 24 (1999) 191–209.
- [20] M. Jiang, H. Yu, D. Harris, Bond rolling resistance and its effect on yielding of bonded granulates by DEM analyses, *International Journal for Numerical and Analytical Methods in Geomechanics* (2006) in press.
- [21] N. Estrada, A. Taboada, F. Radjai, Shear strength and force transmission in granular media with rolling resistance, *Physical Review E* 78, (021301) (2008) 1–11.
- [22] J. Crank, *The mathematics of diffusion*, Oxford university press, Oxford, 1956.
- [23] A. Taboada, N. Estrada, F. Radjai, Additive decomposition of shear strength in cohesive granular media from grain-scale interactions, *Phys Rev Lett* 97, (2006) 098302.
- [24] E. J. Tarbuck, F. K. Lutgens, *Earth – An introduction to Physical Geology*, Pearson Education, New Jersey, 2005.
- [25] V. Topin, J.-Y. Delenne, F. Radjai, L. Brendel, F. Mabilie, Strength and fracture of cemented granular matter, *The European Physical Journal E*, 23 (2007) 413–429.
- [26] V. Topin, F. Radjai, J.-Y. Delenne, A. Sadoudi, F. Mabilie, Frédéric, Wheat endosperm as a cohesive granular material, *Journal of Cereal Science*, 47 (2008) 347–356.

- [27] E., Schlangen, J. G. M., van Mier, Experimental and numerical analysis of micromechanisms of fracture of cement-based composites, *Cement and Concrete Composites*, 14 (1992) 105–118.
- [28] V. Topin, F. Radjai, J.-Y. Delenne, F. Mabilie, Mechanical modeling of wheat hardness and fragmentation, *Powder Technology*, (2008).
- [29] V. Richefeu, F. Radjai, M. S. El Youssoufi, Stress transmission in wet granular materials, *The European Physical Journal E - Soft Matter*, 21 (2006) 359–369.
- [30] C. Voivret, F. Radjai; J.-Y. Delenne, M. S. El Youssoufi, Multiscale force networks in highly polydisperse granular media, *Phys. Rev. Lett.* 102 (2009) 178001.
- [31] L. Bocquet and E. Charlaix and F. Restagno, Physics of humid granular media, *C. R. Physique*, 3 (2002) 207–215.
- [32] S. Herminghaus, Dynamics of wet granular matter, *Adv. Phys.*, 54 (2005) 221–261.
- [33] G. Lian, C. Thornton, M.J. Adams, Discrete Particle Simulation of Agglomerate Impact Coalescence, *Chemical Engineering Science*, 53 (1998) 3381–3391.